AGU PUBLICATIONS

JGR

Journal of Geophysical Research: Solid Earth

RESEARCH ARTICLE
10.1002/2017JB014100

Key Points:
- A sporadic low-velocity layer immediately above the 410 km discontinuity is observed worldwide
- The low-velocity layer covers 33–50% of the resolved region across the Pacific
- The inferred partial melting above the mantle transition zone shows strong heterogeneities

Supporting Information:
- Supporting Information S1

Correspondence to:
S. S. Wei,
shawnwei@ucsd.edu

Citation:
Wei, S. S., and P. M. Shearer (2017), A sporadic low-velocity layer atop the 410 km discontinuity beneath the Pacific Ocean, *J. Geophys. Res. Solid Earth*, *122*, doi:10.1002/2017JB014100.

Received 14 FEB 2017
Accepted 14 JUN 2017
Accepted article online 23 JUN 2017

A sporadic low-velocity layer atop the 410 km discontinuity beneath the Pacific Ocean

S. Shawn Wei[1] **and Peter M. Shearer**[1]

[1]Institute of Geophysics and Planetary Physics, Scripps Institution of Oceanography, University of California, San Diego, La Jolla, California, USA

Abstract Waveforms of *SS* precursors recorded by global stations are analyzed to investigate lateral heterogeneities of upper mantle discontinuities on a global scale. A sporadic low-velocity layer immediately above the 410 km discontinuity (LVL-410) is observed worldwide, including East Asia, western North America, eastern South America, the Pacific Ocean, and possibly the Indian Ocean. Our best data coverage is for the Pacific Ocean, where the LVL-410 covers 33–50% of the resolved region. Lateral variations of our LVL-410 observations show no geographical correlation with 410 km discontinuity topography or tomographic models of seismic velocity, suggesting that the LVL-410 is not caused by regional thermal anomalies. We interpret the LVL-410 as partial melting due to dehydration of ascending mantle across the 410 km discontinuity, which is predicted by the transition zone water filter hypothesis. Given the low vertical resolution of *SS* precursors, it is possible that the regions without a clear LVL-410 detection also have a thin layer. Therefore, the strong lateral heterogeneity of the LVL-410 in our observations suggests partial melting with varying intensities across the Pacific and further provides indirect evidence of a hydrous mantle transition zone with laterally varying water content.

1. Introduction

The mantle transition zone (MTZ), bounded by the 410 and 660 km seismic discontinuities, plays an important role in Earth's evolution and mantle convection. One critical question is the water content in the MTZ, as wadsleyite and ringwoodite are capable of storing 1–3 wt % water in their crystal structures [*Kohlstedt et al.*, 1996]. The answer remains controversial because only one natural sample of hydrous ringwoodite with ~1 wt % of water has been discovered [*Pearson et al.*, 2014]. Although a few geophysical observations suggest the MTZ next to subducted slabs is hydrated by the slab dehydration [e.g., *Zhu et al.*, 2013], others claim that no water is brought below 400 km depth by subduction [e.g., *Green et al.*, 2010]. A related debate concerns global MTZ water content, as geophysical evidence for high water content (on the order of 0.1 wt %) has been found in the Pacific MTZ [*Huang et al.*, 2005], although *Houser* [2016] suggests a dry MTZ globally with only a few hydrous regions with ~0.6 wt % of water. While it is challenging to directly detect water within the MTZ from a seismological prospective [*Thio et al.*, 2016], indirect evidence of the MTZ water content has been obtained from detailed analyses of the 410 km discontinuity [e.g., *van der Meijde et al.*, 2003].

The seismic discontinuity at 410 km depth is usually attributed to an isochemical phase transformation from olivine to wadsleyite [*Ringwood*, 1975]. In addition to this globally observed feature, a low-velocity layer immediately above the 410 km discontinuity (LVL-410 hereinafter) has been observed regionally in many places. The LVL-410 was initially discovered beneath northeast Asia by *Revenaugh and Sipkin* [1994] using seismic waves reflected at the core-mantle boundary (multiple-*ScS* reverberation). Later seismic studies using a similar technique [*Courtier and Revenaugh*, 2007; *Bagley et al.*, 2009], receiver functions [*Vinnik and Farra*, 2002; *Vinnik et al.*, 2003; *Fee and Dueker*, 2004; *Jasbinsek and Dueker*, 2007; *Vinnik and Farra*, 2007; *Wittlinger and Farra*, 2007; *Leahy*, 2009; *Jasbinsek et al.*, 2010; *Schaeffer and Bostock*, 2010; *Tauzin et al.*, 2010; *Vinnik et al.*, 2010; *Schmandt et al.*, 2011; *Huckfeldt et al.*, 2013; *Bonatto et al.*, 2015; *Morais et al.*, 2015; *Thompson et al.*, 2015; *Liu et al.*, 2016], and body wave triplications [*Song et al.*, 2004; *Gao et al.*, 2006; *Obayashi et al.*, 2006] suggest the widespread existence of this LVL (Figure 1 and supporting information Table S1). In addition, an electromagnetic study in the southwestern U.S. also suggests a layer with high conductivity near the 410 km discontinuity [*Toffelmier and Tyburczy*, 2007].

Based on the assumption of a hydrous MTZ, the transition zone water filter (TZWF) hypothesis [*Bercovici and Karato*, 2003; *Leahy and Bercovici*, 2007] proposes that when the ascending mantle passes through the

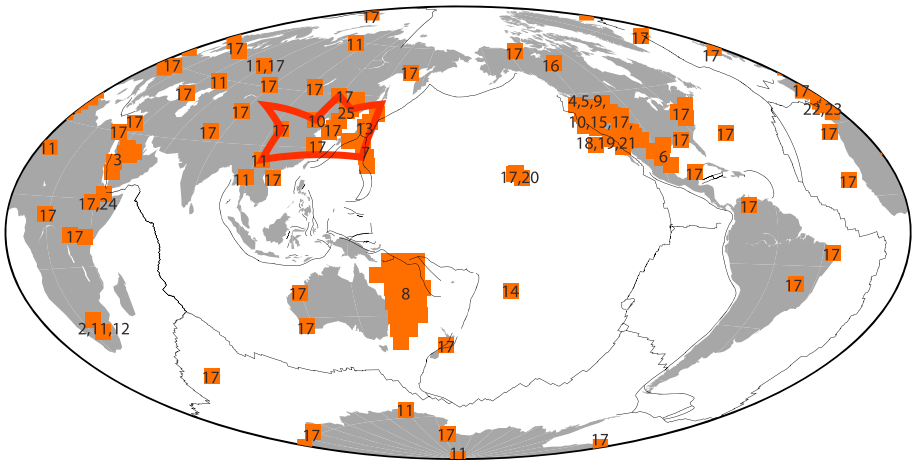

Figure 1. Previous observations of an LVL-410 under continents and continental margins [*Revenaugh and Sipkin*, 1994; *Vinnik and Farra*, 2002; *Vinnik et al.*, 2003; *Fee and Dueker*, 2004; *Song et al.*, 2004; *Gao et al.*, 2006; *Obayashi et al.*, 2006; *Courtier and Revenaugh*, 2007; *Jasbinsek and Dueker*, 2007; *Toffelmier and Tyburczy*, 2007; *Vinnik and Farra*, 2007; *Wittlinger and Farra*, 2007; *Bagley et al.*, 2009; *Leahy*, 2009; *Jasbinsek et al.*, 2010; *Schaeffer and Bostock*, 2010; *Tauzin et al.*, 2010; *Vinnik et al.*, 2010; *Schmandt et al.*, 2011; *Huckfeldt et al.*, 2013; *Tauzin et al.*, 2013; *Bonatto et al.*, 2015; *Morais et al.*, 2015; *Thompson et al.*, 2015; *Liu et al.*, 2016]. Digits indicate the reference numbers listed in supporting information Table S1. The regions of an LVL-410 revealed by receiver function studies are generally beneath the analyzed stations, whereas studies using multiple-*ScS* waves and body wave triplications image large areas with lower resolution. The red polygon in East Asia outlines the region analyzed by *Revenaugh and Sipkin* [1994] using multiple-*ScS* waves.

410 km discontinuity from the hydrous MTZ to the anhydrous upper mantle, wet wadsleyite transforms to dry olivine, releasing water to trigger partial melting above the discontinuity. By invoking a chemical filtering mechanism during dehydration at the 410 km discontinuity, this hypothesis helps resolve the long-standing debate between the whole-mantle-convection model, supported by seismic observations [e.g., *Grand et al.*, 1997], versus the layered-mantle-convection model, inferred from geochemical distinctions between mid-ocean ridge basalts and ocean-island basalts. Therefore, the existence of the LVL-410, indicative of partial melting, is consistent with the TZWF hypothesis and provides indirect evidence for a hydrous MTZ.

However, mantle convection models predict that ascending mantle should cross the 410 km discontinuity in many different regions, and thus, the TZWF should produce a widespread LVL-410, whereas almost all previous observations are confined to continents or continental margins due to limited seismic raypath coverage. Better coverage in oceanic regions can be provided by *SS* precursors (*SdS*), the underside *S* wave reflections off the *d*-km discontinuity, which sample the upper mantle midway between sources and receivers (Figure 2a) and have been widely used to map mantle discontinuity topography [e.g., *Flanagan and Shearer*, 1998; *Chambers et al.*, 2005]. Here we analyze *S410S* waveforms to investigate lateral heterogeneities of the 410 km discontinuity and the potential LVL-410 on a global scale.

2. Data and Methods

2.1. Data Processing and Stacking

Stacking is required to enhance the *SS* precursor signals, which are usually weak and buried in noise. We stack all seismic data recorded by global permanent stations from 1976 to 2010 in a similar manner to *Shearer* [1991], binning the data by bouncepoint to study lateral variations of upper mantle structure. Larger bouncepoint caps include more data and thus yield more reliable stacked waveforms but provide lower lateral resolution.

The stacking was restricted to earthquakes shallower than 75 km depth to reduce complications owing to depth phases. Each transverse-component seismogram was band-pass filtered between 15 and 100 s (first-order Butterworth, zero-phase shift), and then the *SS* phase was automatically picked by searching for the maximum amplitude around the predicted *SS* arrival time according to the IASP91 model [*Kennett and Engdahl*, 1991]. We discarded seismograms with signal-to-noise ratios of *SS* lower than 3 and restricted the source-receiver distance to 106°–176° to avoid interference from *Ss660s*. These restrictions led to 48,180 useable *S410S* traces, which primarily sample the Pacific Ocean and northeast Asia (Figure 3a). Each trace was

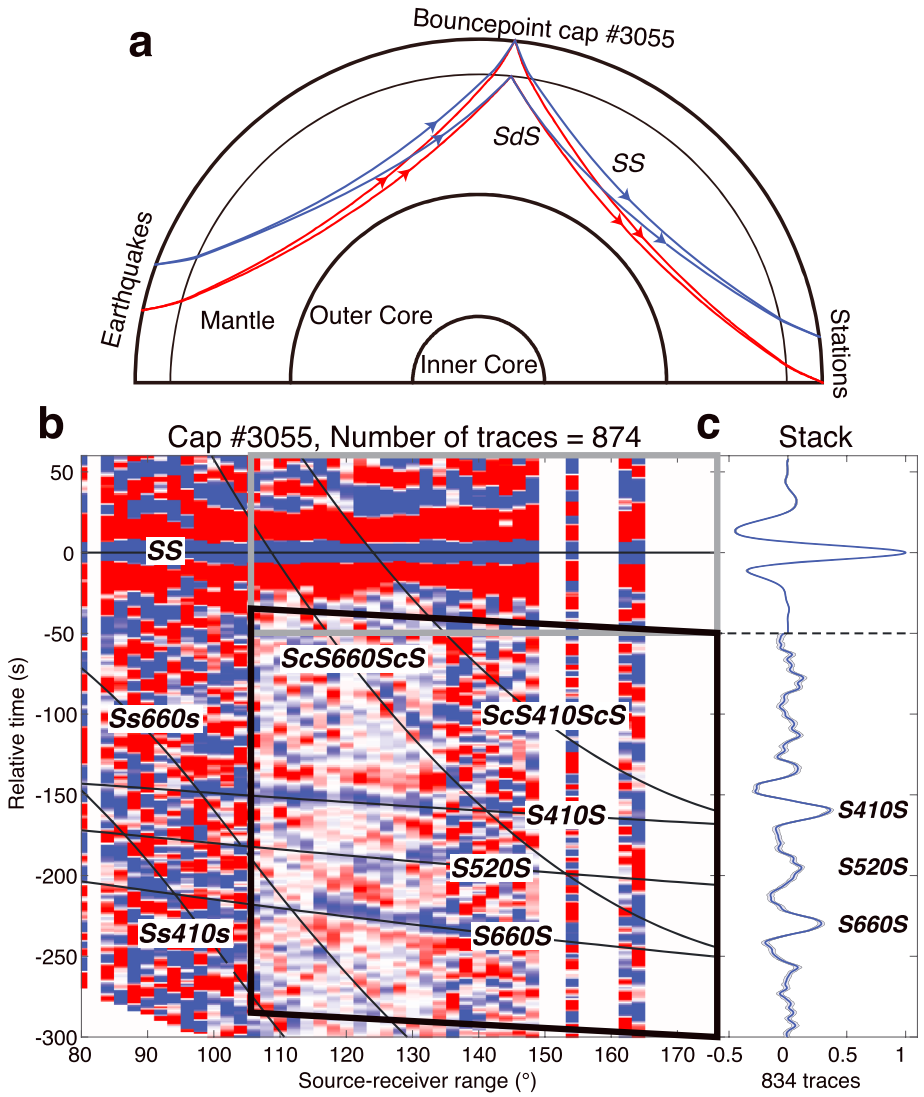

Figure 2. *SS* precursor stacks. (a) Two pairs of *SS* (surface-reflected *S* wave) and precursor *SdS* (underside *S* wave reflection off the *d*-km discontinuity) sharing the same bouncepoint cap. (b) The 874 transverse-component seismograms stacked in one cap aligned to the reference phase *SS*, with positive amplitudes in blue and negative in red. Black curves show the predicted traveltime curves based on the IASP91 model [*Kennett and Engdahl*, 1991]. Grey and black boxes surround 834 seismograms stacked in Figure 2c. *SS* waves are stacked along 0 s (grey box), whereas precursors are stacked along the predicted *S410S* traveltime curve (black box). (c) Seismogram stacks at ranges of 106°–176°. The precursor phases have much smaller amplitudes, and the scale below the thin dashed line is enlarged by 5 times. The 95% confidence limits for the *SS* precursor stacks are shaded in blue, and the 95% confidence limits for the *SS* stacks are within the curve thickness.

normalized and aligned to the maximum *SS* amplitude and then stacked in bouncepoint caps to obtain reference *SS* waveforms. The polarity of each seismogram is switched if necessary so that the *SS* peak amplitude (normalized to unity) is always larger in magnitude than its negative sidelobes. This empirical procedure avoids the need to use earthquake source information, while preserving amplitude and polarity information relative to the reference phase. This simple waveform alignment procedure is easier to implement than reference phase deconvolution or cross-correlation methods [e.g., *Gu et al.*, 1998, 2003] but yields very similar results [*Houser et al.*, 2008]. We stack *S410S* waveforms in a similar manner but aligned to the predicted *S410S* arrival time curve relative to *SS*. Figure 2b shows 874 seismograms sharing a single bouncepoint cap of 5° radius, aligned on the *SS* phase, and stacked as a function of source-receiver distance. Although the results at any particular distance are noisy and often biased by interfering seismic phases, by stacking all of the traces over distances from 106° to 176°, the mantle discontinuity reflections can be clearly resolved (Figure 2c).

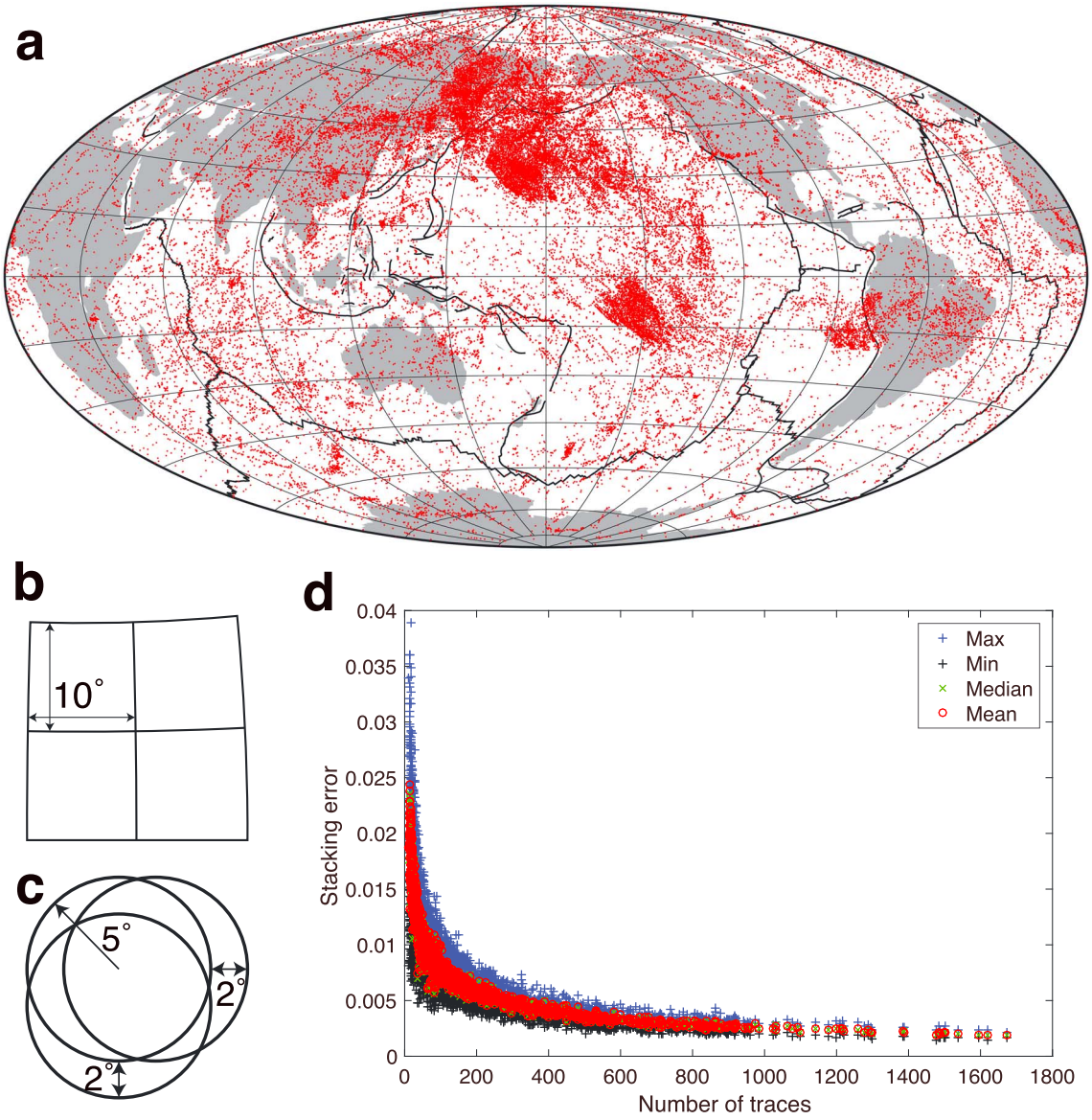

Figure 3. (a) Bouncepoints of all *S410S* seismograms used in this study. (b) Shape of the nonoverlapping bouncepoint caps of ~10° width used for all global surveys. (c) Shape of the overlapping bouncepoint caps of 5° radius and 2° spacing used for the detailed survey of the Pacific Ocean. (d) Stacking errors decrease with increasing numbers of stacked traces in the Pacific survey. Waveform uncertainties are estimated with bootstrap resampling. The stacking error is defined as the average waveform uncertainty over time between −5 and 20 s relative to the *S410S* arrival time because the right sidelobe is our focus. The median, maximum, and minimum waveform uncertainty in each cap are also shown for comparison. The stacks become reliable when the trace number is larger than ~300.

In order to study global variations of the 410 km discontinuity, we first stacked all traces in 412 nonoverlapping bouncepoint caps of ~10° width (Figure 3b) because this technique can only resolve lateral heterogeneities larger than 500–750 km at this depth [*Schmerr et al.*, 2013]. Because the data coverage across the Pacific Ocean is higher and the stacking is more coherent, we further stacked traces in 2000 overlapping bouncepoint caps of 5° radius and 2° spacing across the Pacific Ocean (Figure 3c), which yields smoother images of small-scale features. The uncertainties of the stacked waveform amplitudes were estimated using a bootstrap resampling method [*Efron and Tibshirani*, 1991] where we repeated the stacking 200 times using random subsets of the data. The stacking error in each bouncepoint cap is defined as the average uncertainty over time between −5 and 20 s relative to the *S410S* arrival time since the right sidelobe is our focus as discussed later. As expected, more traces produce more robust stacked waveforms with smaller errors (Figure 3d), and there is no significant reduction in stacking error when the number of stacked traces is

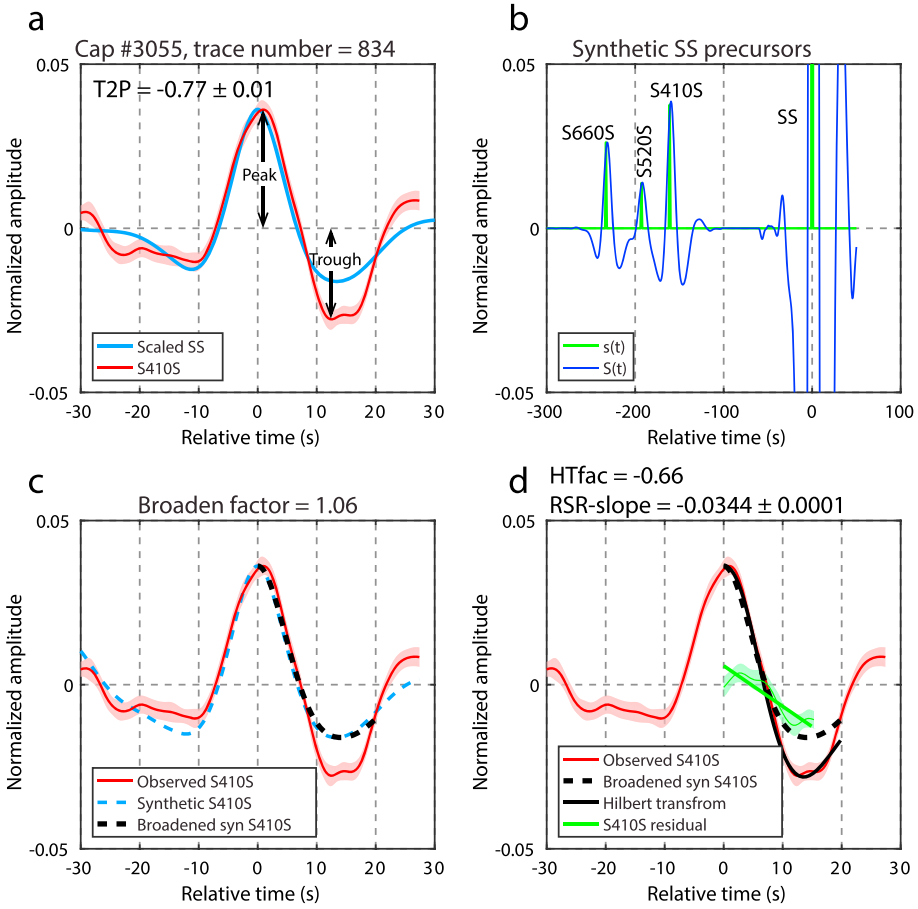

Figure 4. *S410S* waveform analysis. (a) Scaled *SS* (blue) and *S410S* (red) waveforms stacked in cap #3055 (see Figure 7 for its location). In general, structural perturbations at depths below the discontinuity will affect the waveform shape at negative times, whereas perturbations above the discontinuity will change the pulse shape at positive times. The 95% confidence limits for the *S410S* stacks are shaded in pink, and the 95% confidence limits for the *SS* stacks are within the curve thickness. The trough-to-peak ratio (T2P) is defined as the trough amplitude divided by the peak amplitude, and its uncertainty is estimated based on the *S410S* amplitude uncertainties. (b) The discontinuity operators (green) are calculated from the IASP91-LS06 model. The synthetic seismogram (blue) is obtained by convolving the reference *SS* waveform with the discontinuity operators. (c) The synthetic *S410S* waveform from Figure 4b is broadened or narrowed to fit the observed one. (d) The RSR slope is defined as the slope of the *S410S* residuals (green) compared to the stretched synthetic waveform (black dashed) and then is normalized to the *SdS* peak amplitude. The 95% confidence limits for the residuals are shaded in green, which leads to the estimation of the RSR slope uncertainty. The Hilbert transform is applied on the stretched synthetic waveform. The Hilbert transform factor (HTfac) is grid searched for the minimum misfit between the transformed (black solid) and observed (red) waveforms.

larger than ~300. We thus conclude that ~300 traces in each cap are roughly enough to obtain a robust waveform stack with relatively small uncertainties. Accordingly we assign greatest weight to stacks with more than 300 traces, and caps with fewer than 100 traces are discarded. The *S660S* waveforms are obtained in a similar way except that the source-receiver distance was restricted to 120°–176°, and the stacking was along the predicted *S660S* travel-time curve.

2.2. Synthetic Waveform Modeling

We compare our observed *SdS* stacks with predicted *SdS* synthetic waveforms, computed using geometrical ray theory and by convolving the reference phase with discontinuity operators (Figure 4b). Ray theory is sufficiently accurate to capture the main features of interest in our study because we consider only 1-D models, and we window *SS* and its precursors to epicentral distances that exclude complications from triplicated or diffracted phases. The reference velocity model is obtained by modifying the IASP91 model [*Kennett and Engdahl*, 1991] with sharp discontinuities constrained by *Lawrence and Shearer* [2006] (IASP91-LS06

model) to better model the *S520S* phase that may affect the *S410S* waveform. The discontinuity operators are calculated from reflection coefficients and geometric spreading according to this model [*Shearer*, 1996]. Seismic attenuation is ignored, because the *SdS* amplitude and width are not our focus (as discussed in supporting information Text S1). The *SS* waveform stacked in the same bouncepoint cap is used as the reference phase for the convolution in most of the later analyses. Although individual *SS* waveforms vary in shape and symmetry, owing to the effects of depth phases, Moho reflections, and the fact that *SS* is Hilbert transformed relative to direct *S* [*Choy and Richards*, 1975], our alignment and stacking procedure produces a relatively symmetric and repeatable reference *SS* pulse [e.g., *Shearer*, 1991]. However, because the *SS* reference pulse is usually not perfectly symmetric, we need to consider the effects of reference pulse asymmetries on the *SdS* observations and synthetics. Thus, for comparison, we also produce a symmetric reference phase for use in computing *SdS* synthetics by stacking all *SS* waveforms and averaging the left and right sidelobes (Figure S1a).

2.3. Waveform Shape Analysis

After obtaining the *SS* and *SdS* waveforms and calculating the synthetic *SdS* waveforms in each bouncepoint cap, the *SS* amplitude is scaled to the *SdS* amplitude and then aligned along the peaks. For many caps, we find significant differences between the observed *S410S* waveform shapes and the model predictions, in contrast to the *S660S* waveforms, which generally agree more closely with the synthetic waveforms. These *S410S* waveform shape anomalies are the focus of this study, and we will show how they can be related to the likely presence of the LVL-410.

Since the amplitude and relative time of *S520S* can distort the left sidelobe of the *S410S* waveform, we focus on the *S410S* right sidelobe and experiment with three different ways to measure its behavior relative to *SS*:

1. We define the trough-to-peak ratio (T2P) of *SdS* as the trough amplitude of the right sidelobe divided by the peak amplitude (Figure 4a). The T2P error is estimated based on the trough and peak amplitude uncertainties of the *SdS* stack.
2. The synthetic *SdS* waveform based on the IASP91-LS06 model is first broadened or narrowed to match the observed *SdS* width (Figure 4c). We then apply a Hilbert transform approach to distort the broadened/narrowed synthetic *SdS* waveform to fit the right sidelobe of the observed *SdS*. The resulting waveform is a combination of a $-\pi/2$ Hilbert-transformed and a $\pi/2$ Hilbert-transformed pulse with a weighting factor ranging from -1 to 1. This weighting factor, Hilbert transform factor (HTfac), is grid searched for the minimum misfit between the synthetic and observed waveforms (Figure 4d).
3. We calculate the residuals of the observed *SdS* waveform compared to the broadened/narrowed synthetic waveform and define the Right-Sidelobe-Residual slope (RSR slope) as the slope of the residuals from 0 to 15 s. This RSR slope is normalized to the *SdS* peak amplitude in order to extract the relative information between the trough and the peak. The RSR slope uncertainty is estimated as the model error of the linear regression. These analyses are applied to the *S410S* and *S660S* waveforms stacked in all caps with more than 100 traces.

3. *SdS* Waveform Shape

The stacked *S410S* and *S660S* waveform shapes show significant variations, whereas the stacked *SS* waveforms are generally consistent and nearly symmetric (Figures 5 and S2). One obvious feature is that *S410S* waveforms stacked in many caps are asymmetric with a deep trough in the left or right sidelobe (Figures 6a and S2). Although the left sidelobe of long-period *S410S* can be affected by *S520S*, the right sidelobe should be stable for a simple 410 km discontinuity. Thus, we focus on the shape of the right sidelobe instead of the total waveform symmetry.

The skewed *S410S* waveforms are unlikely to be an artifact due to data filtering or stacking techniques. Figures S3a and S3b show the *S410S* waveforms stacked using the same seismograms as in Figure 6a but with different filters. Despite the appearance of short-wavelength wiggles, it is clear that the right sidelobe is much stronger, which is indicated by the negative RSR slope. Additionally, the *SdS* waveform will be slightly distorted from stacking over varying source-receiver distances, because the relationship between time and discontinuity depth is slightly nonlinear. To avoid this distortion, we convert all seismograms used in Figure 6a from time to depth based on the IASP91 model prior to stacking. The stacked waveform, which

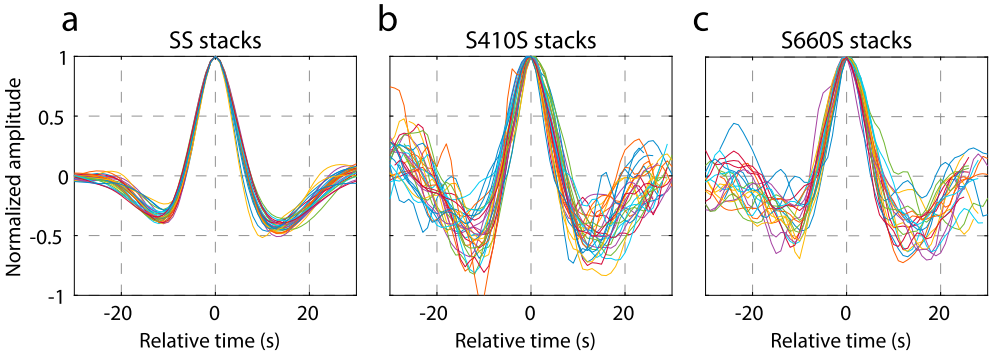

Figure 5. Waveform comparisons in the global survey. (a) *SS* stacks in nonoverlapping caps with more than 300 traces. (b) *S410S* stacks in nonoverlapping caps with more than 300 traces. (c) *S660S* stacks in nonoverlapping caps with more than 300 traces. See Figure S2 for individual waveforms.

is a function of depth, is almost identical with the waveform stacked in the time domain (Figure S3c). However, this conversion relies on the velocity model and thus may introduce other waveform distortions. So for simplicity, we focus our analyses and discussions on the waveforms stacked in the time domain.

The three different measures of *S410S* waveforms correlate well with each other in a detailed study across the Pacific Ocean using overlapping bouncepoint caps (Figures 7b and 8). We prefer the RSR slope measure because it has smaller uncertainties (notice the standard deviations of T2P and RSR slope in Figure 6) and is more robust with respect to short-wavelength wiggles in the waveform stacks. A negative RSR slope indicates a strong right sidelobe of *S410S*, and a positive RSR slope, which is seen occasionally, reflects short-wavelength wiggles in the right sidelobe (Figure 6).

Figure 7a shows the *S410S* RSR slope in each bouncepoint cap in a global survey, and a more detailed study across the Pacific Ocean is shown in Figure 7b. Strong negative RSR slopes are observed sporadically across the Pacific, northeast Asia, and South America. Could the negative *S410S* RSR slope be explained as contamination from other phases or systematic variations in the reference *SS* waveforms? First, since the raypaths of

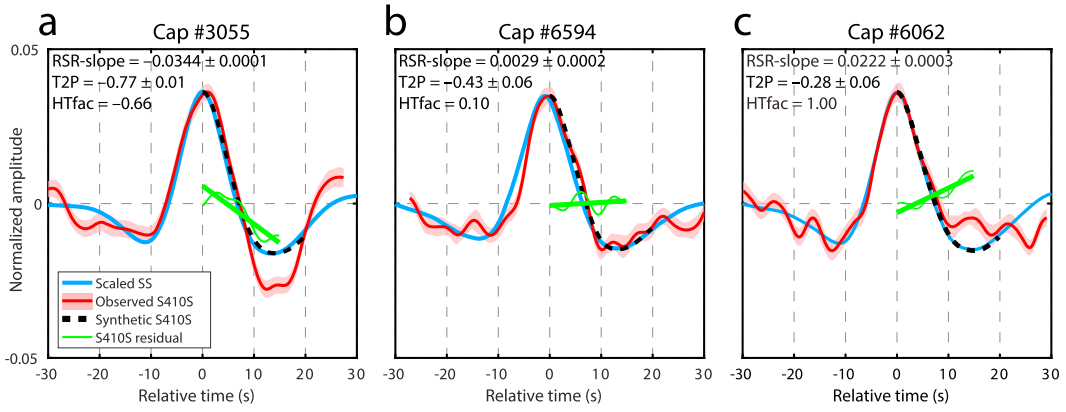

Figure 6. Examples of *S410S* waveforms stacked in 5° radius caps. (a) Stacked waveforms for a cap in the northwest Pacific. The *SS* waveform is nearly symmetric, whereas the *S410S* waveform is asymmetric, suggesting anomalous structure near 410 km depth. (b) Stacked waveforms for a cap in the South Pacific. The *SS* and *S410S* waveforms are similar and nearly symmetric. (c) Stacked waveforms for a cap in the south Pacific. The RSR slope is positive due to short-wavelength wiggles in the *S410S* right sidelobe. The cap locations are shown in Figure 7. The *SS* amplitude (blue) is scaled to the *S410S* amplitude (red), and their peaks are aligned. The 95% confidence limits for the *S410S* stacks are shaded in pink. The black dashed curve indicates the synthetic *S410S* waveform calculated from the reference *SS* waveform. The thin green line plots the residuals of the observed *S410S* waveform compared to the synthetic one; its slope (thick green line) defines our *S410S* RSR slope measure. RSR slope, HTfac, and T2P are measured in the same way as in Figure 4. A negative RSR slope indicates an anomalously deep *S410S* right sidelobe, whereas a positive RSR slope is caused by short-wavelength wiggles in the right sidelobe.

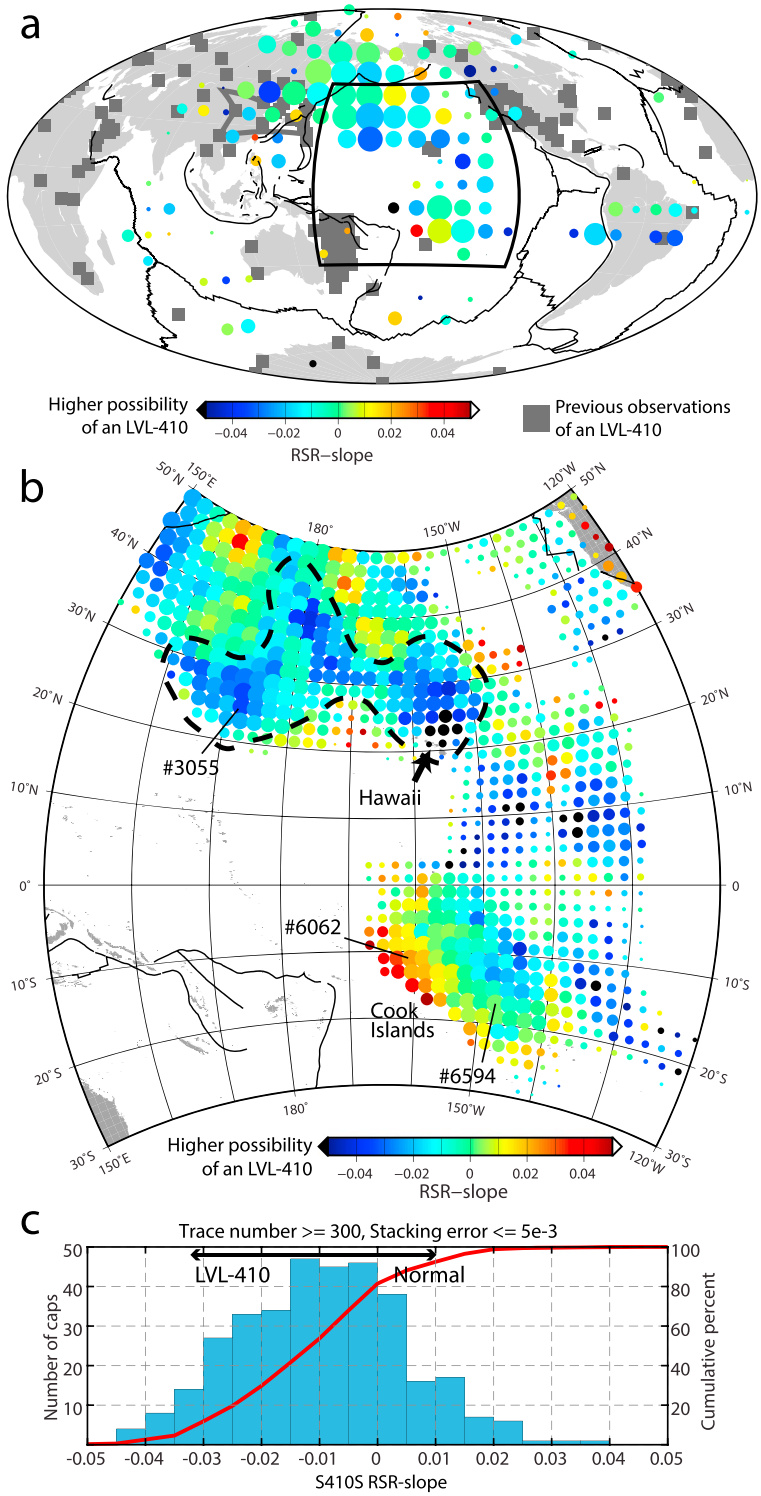

Figure 7. Maps of *S410S* RSR slope. (a) A global survey for nonoverlapping bouncepoint caps of ~10° width (Figure 3b). Thin black curves indicate plate boundaries. Bold black curves outline the region in Figure 7b. Dark grey squares indicate previous observations of an LVL-410 (Figure 1). (b) A more detailed survey across the Pacific Ocean using overlapping caps of 5° radius and 2° spacing. Only caps with more than 100 seismograms are shown in Figures 7a and 7b, and circle sizes are scaled to emphasize reliable caps according to their stacking errors. Numbers show the example cap locations in Figures 2, 4, and 6. Larger negative skewness anomalies provide stronger evidence for a low-velocity layer atop the 410 km discontinuity (LVL-410). (c) Histogram of *S410S* skewness shown in Figure 7b. The red curve indicates cumulative percentage. Only caps with more than 300 seismograms and stacking error smaller than 5e−3 are included.

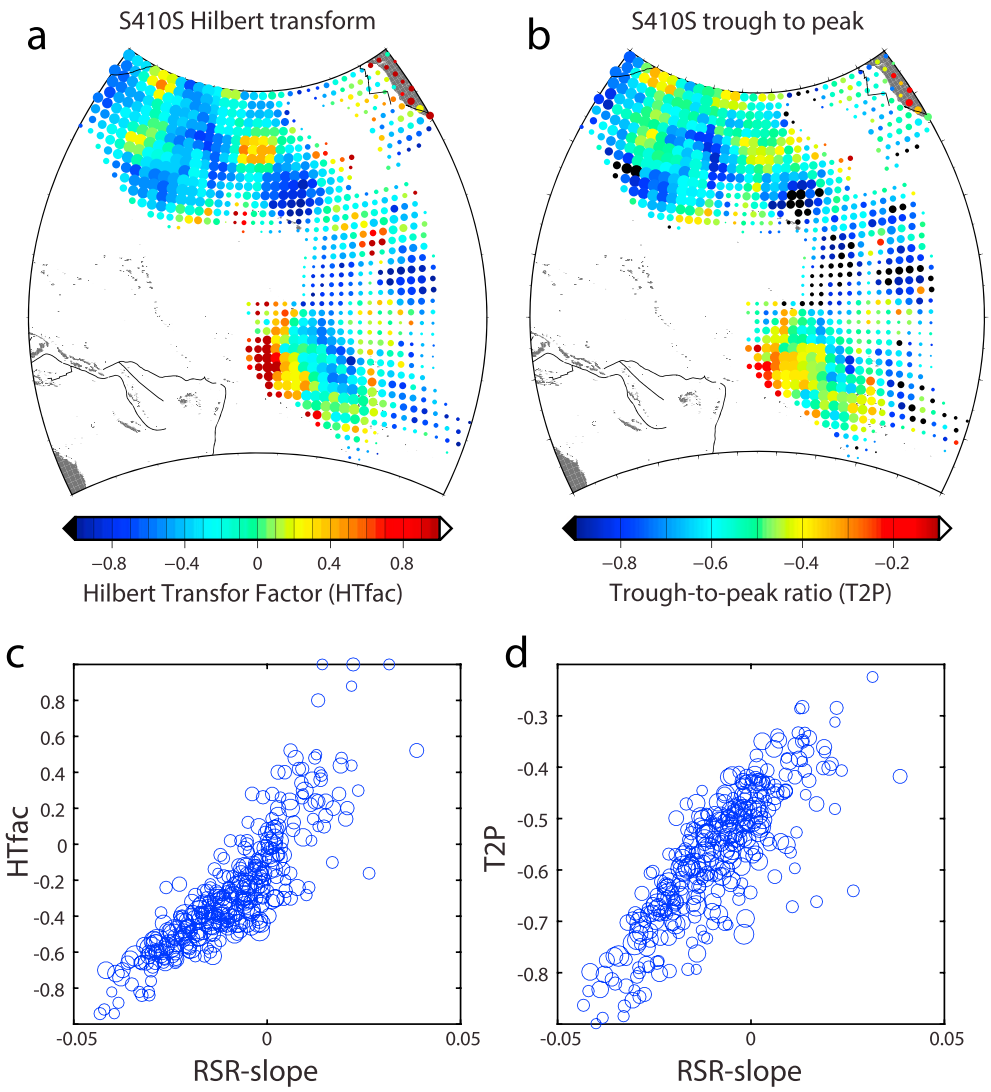

Figure 8. Maps of *S410S* (a) Hilbert transform factor and (b) trough-to-peak ratio as defined in Figure 4 for the Pacific Ocean. Plots are similar to Figure 7b. (c, d) *S410S* RSR slope generally correlates well with HTfac and T2P. Circle sizes are scaled to emphasize reliable caps according to their stacking errors.

SdS and *SS* are almost identical away from the bouncepoint, source differences including depth phases should distort both *SS* and *SdS* waveforms in the same way and thus have little influence on the *SdS* RSR slope. Second, the Moho beneath the bouncepoint may amplify the right sidelobe of the reference *SS* waveform [*Shearer*, 1996], which in turn diminishes the negative *SdS* RSR slope. The map of *S410S* RSR slope calculated from a symmetric reference phase (Figure S1c) shows little difference from the map using the *SS* waveform stacked in each bouncepoint cap (Figure 7a). Third, similar analyses on *SS* and *S660S* waveforms show that the *SS* and *S660S* shapes have no systematic correlation with the *S410S* RSR slope across the Pacific Ocean (Figure 9) or on a global scale (Figure 10). Fourth, we stacked *SS*, *S410S*, and *S660S* traces in "negative" Pacific caps (with *S410S* RSR slope smaller than −0.01) and in all other Pacific caps. The right sidelobes of the stacked *SS* and *S660S* waveforms are consistent, whereas the *S410S* waveforms show obvious variations (Figure 11). Fifth, the RSR slope uncertainties obtained from bootstrap resampling are much smaller than the observed RSR slope anomalies (Figure S4). Finally, although incoherent stacking can change the *SdS* waveform amplitude and width, it produces negligible bias on the *SdS* RSR slope, especially in oceanic regions (supporting information Text S1 and Figure S5). Therefore, we conclude that the strong negative anomalies of *S410S* RSR slope across the Pacific Ocean are robust, and those in northeast Asia and South America are likely also present.

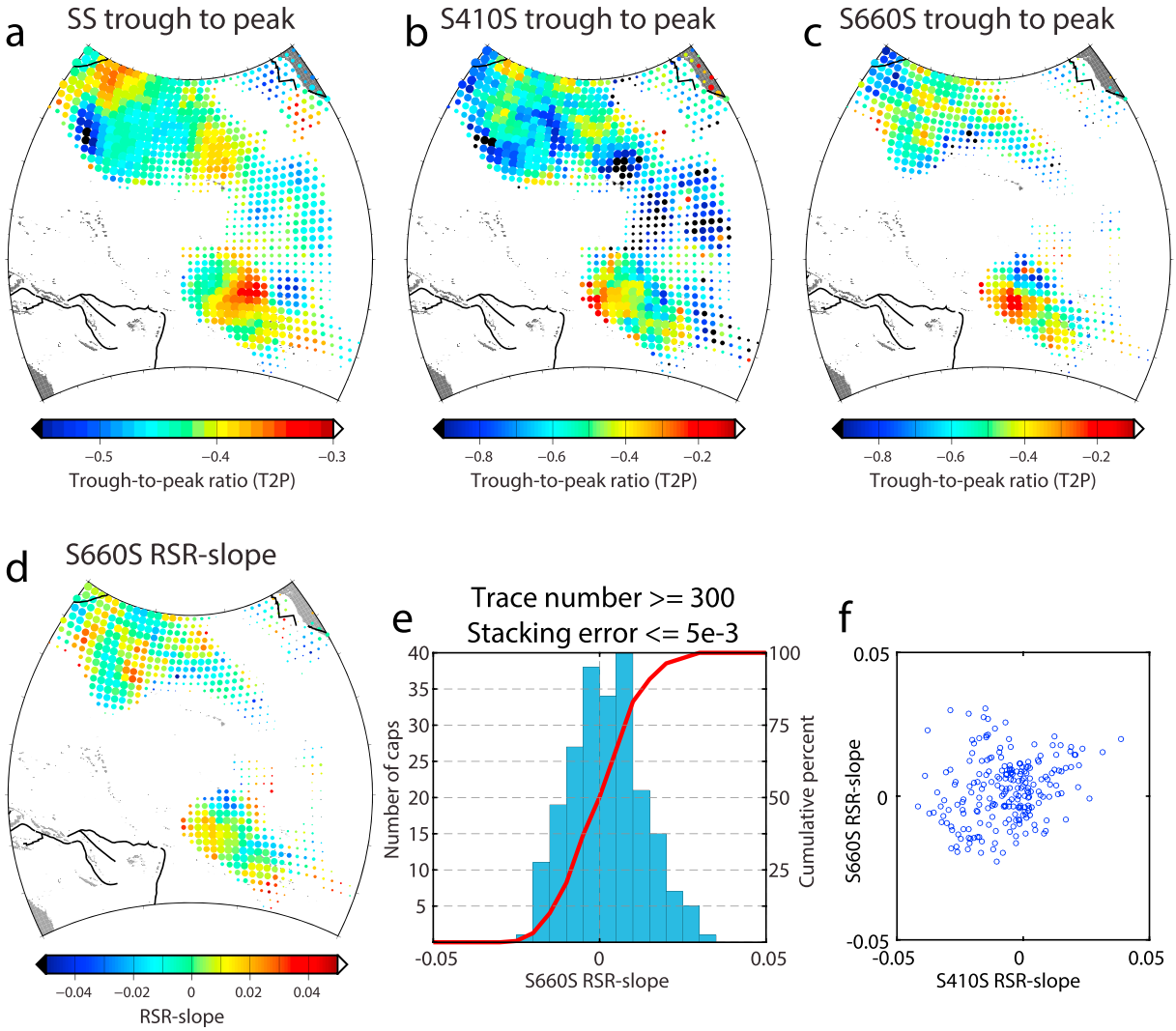

Figure 9. (a–c) Pacific maps of *SS*, *S410S*, and *S660S* trough-to-peak ratio. They show no systematic correlation with each other. Circle sizes are scaled to emphasize reliable caps according to their stacking errors. (d) Pacific map of *S660S* RSR slope, showing different patterns compared to *S410S* RSR slopes in Figure 7b. (e) Histogram of *S660S* RSR slopes across the Pacific Ocean, in comparison with Figure 7c. (f) Little correlation is seen between *S410S* and *S660S* RSR slope measurements across the Pacific Ocean.

4. Discussions

4.1. Low-Velocity Layer Atop the 410 km Discontinuity

The strong *S410S* negative RSR slope, i.e., the deep trough of the right sidelobe, is unexpected for a simple 410 km discontinuity, as shown by a synthetic *S410S* waveform calculated from the IASP91-LS06 model (Figure 12). The most likely explanation is structure near 410 km depth, i.e., the LVL-410 suggested by previous studies (Figure 1). In order to quantify the LVL characteristics, we conduct a series of modeling tests to fit an example *S410S* waveform in one of the bouncepoint caps with the strongest LVL-410 signals (Figure 12). By parameterizing the LVL as a negative-gradient discontinuity with a finite thickness immediately above the 410 km discontinuity, we grid search for the 410 km discontinuity thickness (D_{410}, 0 to 50 km), the LVL thickness (D_{LVL}, 0 to 80 km), and the impedance (product of density and velocity) contrast ratio (Z_{LVL}/Z_{410}, −50% to 50%) to invert for the best velocity and density models. The density and velocity values at the top of the LVL-410 and at the bottom of the 410 km discontinuity are fixed to the IASP91 model [*Kennett and Engdahl*, 1991]. The best fitting model shows a strong LVL-410 with a thickness of 26 km and a shear wave velocity reduction as great as 10% in a cap characterized by an extremely negative RSR slope. A "good" model is defined as a model whose corresponding *S410S* waveform misfit is smaller than twice the

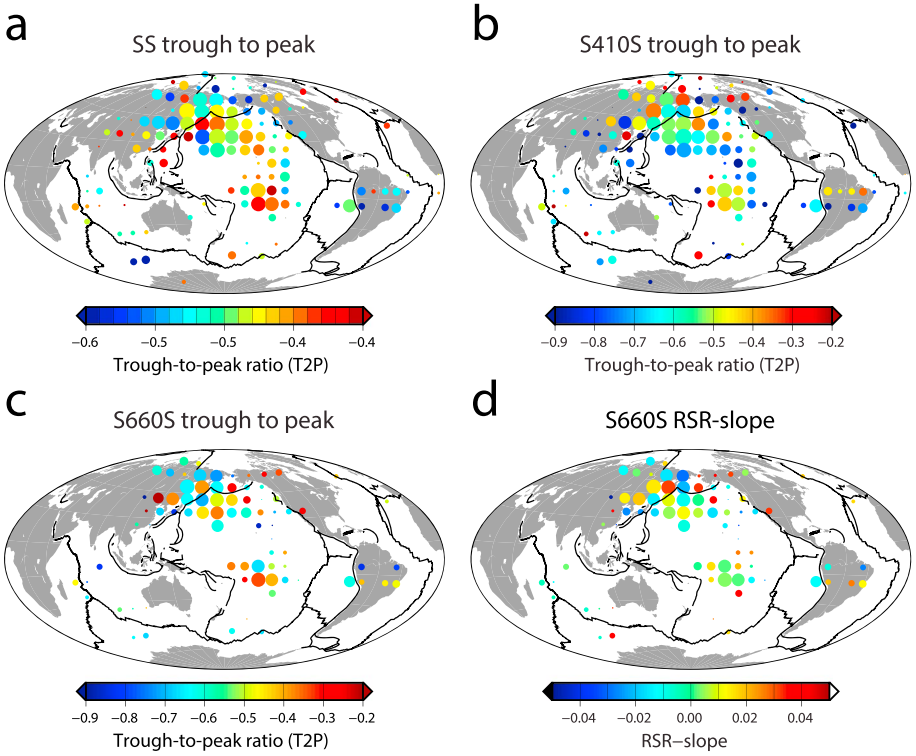

Figure 10. (a–c) Global maps of *SS*, *S410S*, and *S660S* trough-to-peak ratio. They show no systematic correlation with each other. Circle sizes are scaled to emphasize reliable caps according to their stacking errors. (d) Global map of *S660S* RSR slope, showing different patterns compared to *S410S* RSR slopes in Figure 7a.

misfit for the best fitting model. Then the velocity and density uncertainties are estimated based on these "good" models. Compared to previous studies with a 3–8% velocity reduction and thickness varying from 20 to 80 km, our results for this extreme example provide an upper bond in velocity reduction but are intermediate in thickness.

Many factors, including incoherent stacking, attenuation, and scattering in the upper mantle, and ray angle, can affect the *S410S* waveform and this inversion. Additionally, the nature of long-period seismic waves, with a wavelength of ~150 km, limits the vertical resolution. In order to test the sensitivity of RSR slope to the thickness and impedance contrast of the LVL-410, we generate synthetic *SdS* waveforms using various parameters

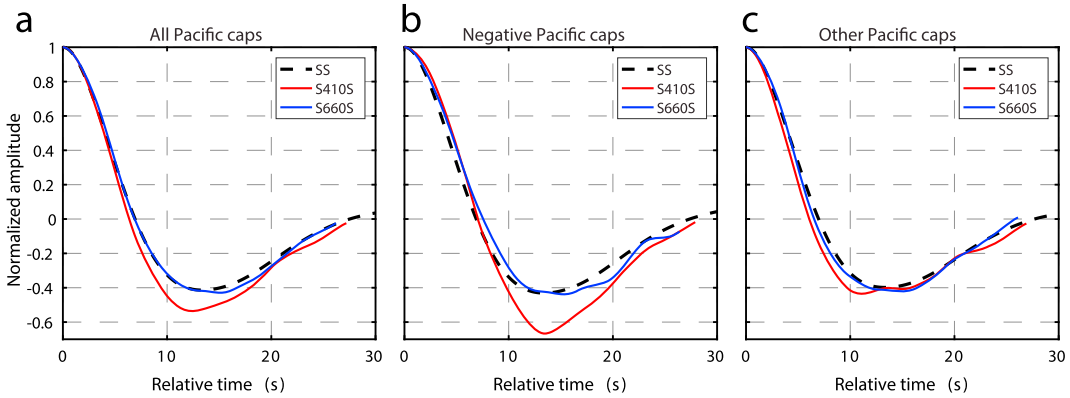

Figure 11. Comparisons of *SS* and *SdS* right sidelobes stacked in nonoverlapping Pacific caps. (a) Right sidelobes of *SS*, *S410S*, and *S660S* stacked in all Pacific caps. (b) Right sidelobes of *SS* and *S660S* stacked in all "negative" Pacific caps (*S410S* RSR slopes smaller than −0.01) are similar, whereas the *S410S* stack is clearly different. (c) Right sidelobes of *SS*, *S410S*, and *S660S* stacked in all other Pacific caps are similar.

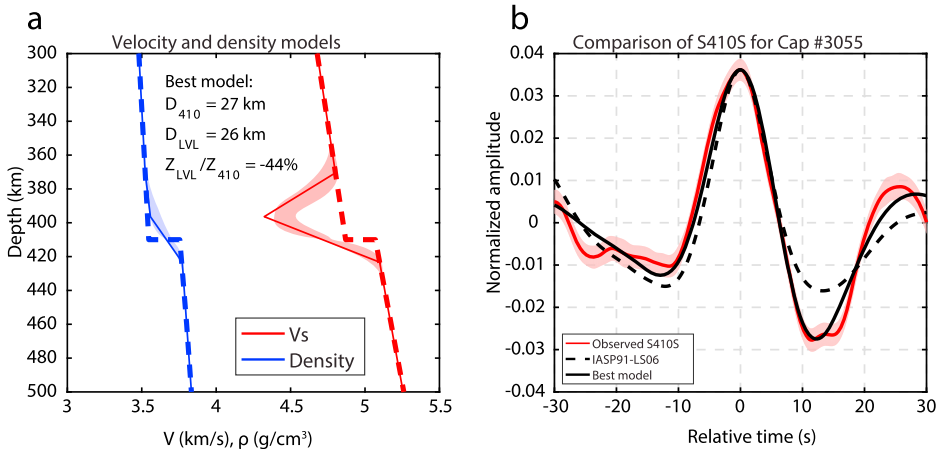

Figure 12. Example of *S410S* waveform modeling. (a) Mantle *S* wave velocity and density models. Dashed lines indicate a modified IASP91 model [*Kennett and Engdahl*, 1991] with sharp discontinuities constrained by *Lawrence and Shearer* [2006] (IASP91-LS06 model). Solid lines show the modified model corresponding to the synthetic waveform that fits the observation best. This model includes a 27 km thick 410 km discontinuity and a 26 km thick LVL-410 whose impedance (*Z*) is −44% of the impedance of the 410 km discontinuity. Pink and light blue shades indicate the uncertainties of velocity and density, respectively. (b) Observed and synthetic *S410S* waveforms. The black dashed curve shows the synthetic waveform produced by the IASP91-LS06 model, whereas the black curve is the best-fitting synthetic waveform based on the modified model plotted in Figure 12a.

and then measure the corresponding values of RSR slope, HTfac, and T2P (Figure 13). These tests suggest that an LVL-410 is always required to model the *S410S* right sidelobe in caps where strong anomalies of negative RSR slope (smaller than −0.02 to −0.01) are observed. Given the large uncertainties in the velocity inversion, it is difficult to quantify the relationship between RSR slope and the LVL-410. Larger negative RSR slopes provide stronger evidence for an LVL-410, but inverting for detailed LVL structure is not warranted given the bandwidth of our data.

Our results unambiguously reveal an LVL-410 distributed sporadically but worldwide (Figure 7a). The existence of the LVL-410 beneath northeast Asia, western North America, eastern South America, and East Antarctica is in general agreement with previous observations in continents and continental margins [*Revenaugh and Sipkin*, 1994; *Song et al.*, 2004; *Jasbinsek and Dueker*, 2007; *Vinnik and Farra*, 2007; *Schaeffer and Bostock*, 2010; *Tauzin et al.*, 2010; *Schmandt et al.*, 2011]. For instance, *Vinnik and Farra* [2007] also observed a strong right sidelobe of *S410p* (*S* wave converted to *P* wave at the 410 discontinuity) and an associated 350 km discontinuity beneath stations BJT and HIA, indicating an LVL-410 beneath northeast China.

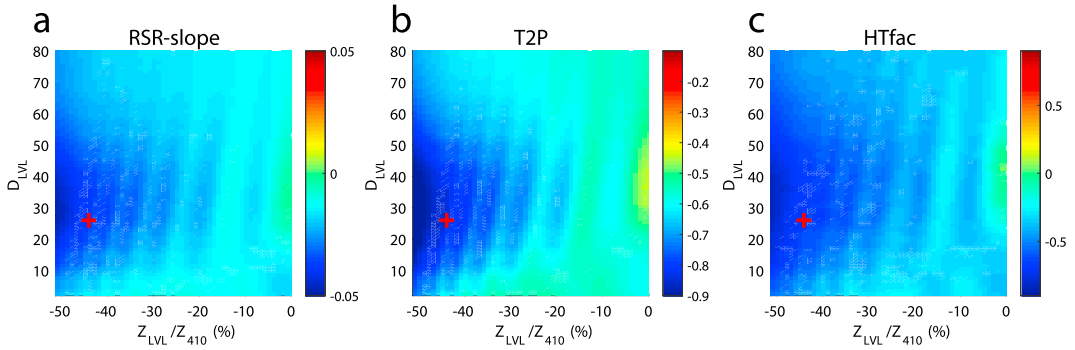

Figure 13. Forward modeling of (a) RSR slope, (b) T2P, and (c) HTfac as a function of the LVL-410 thickness and impedance contrast. The reference phase is the same as the *SS* waveform at Cap #3055 (Figure 4a). The RSR slope, T2P, and HTfac are obtained from a synthetic S410S waveform that is calculated with given values of the LVL-410 thickness and impedance contrast. The 410 km discontinuity thickness is fixed at 30 km as suggested by *Lawrence and Shearer* [2006]. Red crosses indicate the LVL-410 parameters shown in Figure 12a. The existence of an LVL-410 is required when RSR slope < -0.02, T2P < -0.6, and HTfac < -0.4.

The LVL-410 may also exist beneath the Indian Ocean, although the sparseness of data there prevents a solid conclusion. Given the low vertical resolution of our *S410S* data, it is possible that the regions with neutral RSR slope also have an LVL-410, but which is too thin to be observed.

More reliable results are shown for the Pacific (Figure 7b), where we have the most data and where more than 75% of the well-resolved caps are characterized by negative RSR slope (Figure 7c). If we assume the RSR slope uncertainty due to incoherent stacking is about −0.01 (Figure S5c) and consider the large uncertainties of the velocity inversion, we estimate that the LVL-410 covers about 33 to 50% of the resolved area across the Pacific Ocean. The most prominent LVL-410 signal is beneath the northwest Pacific and seems to be clustered into three subregions (outlined by the dashed line in Figure 7b). The LVL-410 beneath Hawaii is not definitive in our results due to the lack of raypath coverage but was suggested by previous receiver function studies using local data [*Tauzin et al.*, 2010; *Huckfeldt et al.*, 2013].

The strong positive RSR slopes at the Northern Cook Islands are puzzling, especially given the fact that an LVL-410 with a thickness of 80 km was detected beneath the Southern Cook Islands [*Leahy*, 2009]. The positive RSR slope is caused by short-wavelength wiggles in the *S410S* waveform (Figure 6c), which are similar to the multiple conversions in the receiver function analysis [*Leahy*, 2009]. We suggest that the LVL-410 in this region may be so thick that the negative signal of the LVL-410 top is separated from the positive signal of the 410 km discontinuity, resulting in short-wavelength wiggles in the *S410S* waveform result. Alternatively, these wiggles may reflect small-scale reflectors in the upper mantle due to chemical heterogeneities introduced by the Cook Island mantle plume [*Montelli et al.*, 2004].

4.2. Partial Melting Above the Mantle Transition Zone

The lateral variations of our LVL-410 observations do not correlate with any available tomographic models of seismic velocity [e.g., *Lebedev and van der Hilst*, 2008; *French and Romanowicz*, 2015] or 410 km discontinuity topography [e.g., *Flanagan and Shearer*, 1998; *Chambers et al.*, 2005], which primarily reflect thermal heterogeneity in the mantle. In addition, likely temperature variations are too small to explain strong reductions in *S* wave velocity [*Takei et al.*, 2014; *Faul and Jackson*, 2015]. Alternatively, the LVL-410 in our results could be modeled as strong anisotropy atop the 410 km discontinuity, because most of the Pacific caps are sampled only by NE-SW striking raypaths. However, this model does not predict the lateral variations across the Pacific, and strong anisotropy is not expected atop the 410 km discontinuity.

The most plausible explanation for our observations is a partial melting layer caused by high water concentration or a combination of high water content and high temperature. Observations of high electrical conductivity and anomalously high Poisson's ratio of the LVL-410 beneath the southwestern U.S. [*Toffelmier and Tyburczy*, 2007] and northwestern Canada [*Schaeffer and Bostock*, 2010], respectively, further confirm the existence of partial melt above the 410 km discontinuity. Due to the low vertical resolution of *SS* precursors and large uncertainties in the velocity inversion, we hesitate to convert our observations of RSR slope to mantle porosity filled with melt. If we assume the maximum shear wave velocity reduction to be 10% (Figure 12) and follow the seismic-physical relationship of *Hier-Majumder and Tauzin* [2017], the upper bond of melt content of the LVL-410 is estimated to be about 4%. However, the largest uncertainty comes from the relationship between seismic velocity and rock physical properties. Recent experiments of polycrystalline borneol aggregates suggest that seismic velocity reductions at near-solidus temperatures are much more significant than previously thought [*Yamauchi and Takei*, 2016], in which case the melt content of our observed LVL-410 may be less than 1%.

Although the LVL-410 and the inferred melting layer near subduction zones can be explained by slab dehydration [e.g., *Song et al.*, 2004], no similar feature is expected beneath the Pacific Ocean. The TZWF hypothesis [*Bercovici and Karato*, 2003] based on the assumption of a hydrous MTZ can solve this discrepancy: when mantle convection drives the ambient mantle upward across the 410 km discontinuity, hydrous wadsleyite transforms to dry olivine, releasing a large amount of water to trigger partial melting. An improved TZWF model [*Leahy and Bercovici*, 2007] suggests that an entrainment mechanism can help melt spreading, which leads to a varying thickness of the melting layer and heterogeneous water content in the MTZ. This model, however, predicts a diminished melting layer near mantle plumes, contrary to previous and our observations [*Tauzin et al.*, 2010; *Huckfeldt et al.*, 2013]. By revisiting water storage capacity in olivine, *Hirschmann* [2006] suggested that partial melting atop the 410 km discontinuity can still exist in hot plumes. Driven by these

arguments, *Schmandt et al.* [2011] attributed the sporadic detection of LVL-410 beneath the western U.S. to small-scale mantle convections that disrupt the melt spreading atop the 410 km discontinuity. The flattening of seafloor bathymetry with age suggests that small-scale mantle convection may exist beneath old ocean plates [*Parsons and Sclater*, 1977; *Huang and Zhong*, 2005]. But there is no direct observational evidence for such small-scale convection in the Pacific mantle. Therefore, the strong lateral heterogeneity of the LVL-410 in our observations suggests partial melting with varying intensities across the Pacific, which may further imply varying water content in the Pacific MTZ.

5. Conclusions

We investigate the substructure of the 410 km discontinuity by stacking and analyzing *SS* precursors recorded by global stations. Incoherent stacking and seismic attenuation can significantly change the *SdS* amplitude and width but have little effect on sidelobe shapes. A large fraction of *S410S* stacks show an anomalously deep trough in the right sidelobe, indicating an LVL-410 beneath those regions, including East Asia, western North America, eastern South America, the Pacific Ocean, and possibly the Indian Ocean, in agreement with previous observations. A detailed survey across the Pacific shows that the LVL-410 covers 33–50% of the resolved region. Due to the low vertical resolution of *SS* precursors, a thin LVL-410 may still exist beneath the other regions. The lateral variations of this LVL-410 show no geographical correlation with tectonic settings, hot spots, 410 km discontinuity topography, or seismic tomography models, suggesting that the LVL is not caused by regional thermal anomalies. We attribute the LVL-410 to a partial melting layer predicted by the transition zone water filter hypothesis. Its lateral variations imply regional heterogeneities of partial melting at the 410 km discontinuity and the inferred dehydration of the MTZ.

Acknowledgments
We thank C.A. Rychert, N. Schmerr, G. Masters, and D. Bercovici for constructive discussions. J.S. Buehler, W. Fan, N.J. Mancinelli, W. Wang, and D.T. Trugman helped to maintain the database of global long-period seismograms. Two anonymous reviewers are appreciated for providing helpful comments to improve this manuscript. This work was made possible by NSF grant EAR-1620251. S.S. W. was supported by the Cecil H. and Ida M. Green Foundation. The authors declare no competing interests. Raw seismic data are available at Data Management Center of Incorporated Research Institutions for Seismology (www.iris.edu/dms/nodes/dmc). Correspondence and requests for materials should be addressed to S.S.W. (shawnwei@ucsd.edu).

References

Bagley, B., A. M. Courtier, and J. Revenaugh (2009), Melting in the deep upper mantle oceanward of the Honshu slab, *Phys. Earth Planet. Inter.*, *175*(3–4), 137–144, doi:10.1016/j.pepi.2009.03.007.

Bercovici, D., and S.-i. Karato (2003), Whole-mantle convection and the transition-zone water filter, *Nature*, *425*(6953), 39–44, doi:10.1038/nature01918.

Bonatto, L., M. Schimmel, J. Gallart, and J. Morales (2015), The upper-mantle transition zone beneath the Ibero-Maghrebian region as seen by teleseismic *Pds* phases, *Tectonophysics*, *663*, 212–224, doi:10.1016/j.tecto.2015.02.002.

Chambers, K., J. H. Woodhouse, and A. Deuss (2005), Topography of the 410-km discontinuity from *PP* and *SS* precursors, *Earth Planet. Sci. Lett.*, *235*(3–4), 610–622, doi:10.1016/j.epsl.2005.05.014.

Choy, G. L., and P. G. Richards (1975), Pulse distortion and Hilbert transformation in multiply reflected and refracted body waves, *Bull. Seismol. Soc. Am.*, *65*(1), 55–70.

Courtier, A. M., and J. Revenaugh (2007), Deep upper-mantle melting beneath the Tasman and Coral Seas detected with multiple *ScS* reverberations, *Earth Planet. Sci. Lett.*, *259*(1–2), 66–76, doi:10.1016/j.epsl.2007.04.027.

Efron, B., and R. Tibshirani (1991), Statistical data analysis in the computer age, *Science*, *253*(5018), 390–395, doi:10.1126/science.253.5018.390.

Faul, U., and I. Jackson (2015), Transient creep and strain energy dissipation: An experimental perspective, *Annu. Rev. Earth Planet. Sci.*, *43*(1), 541–569, doi:10.1146/annurev-earth-060313-054732.

Fee, D., and K. Dueker (2004), Mantle transition zone topography and structure beneath the Yellowstone hotspot, *Geophys. Res. Lett.*, *31*, L18603, doi:10.1029/2004GL020636.

Flanagan, M. P., and P. M. Shearer (1998), Global mapping of topography on transition zone velocity discontinuities by stacking *SS* precursors, *J. Geophys. Res.*, *103*(B2), 2673–2692, doi:10.1029/97JB03212.

French, S. W., and B. Romanowicz (2015), Broad plumes rooted at the base of the Earth's mantle beneath major hotspots, *Nature*, *525*(7567), 95–99, doi:10.1038/nature14876.

Gao, W., E. Matzel, and S. P. Grand (2006), Upper mantle seismic structure beneath eastern Mexico determined from *P* and *S* waveform inversion and its implications, *J. Geophys. Res.*, *111*, B08307, doi:10.1029/2006JB004304.

Grand, S. P., R. D. van der Hilst, and S. Widiyantoro (1997), High resolution global tomography: A snapshot of convection in the Earth, *GSA Today*, *7*(4), 1–7.

Green, H. W., W.-P. Chen, and M. R. Brudzinski (2010), Seismic evidence of negligible water carried below 400-km depth in subducting lithosphere, *Nature*, *467*(7317), 828–831, doi:10.1038/nature09401.

Gu, Y., A. M. Dziewonski, and C. B. Agee (1998), Global de-correlation of the topography of transition zone discontinuities, *Earth Planet. Sci. Lett.*, *157*(1), 57–67, doi:10.1016/S0012-821X(98)00027-2.

Gu, Y. J., A. M. Dziewoński, and G. Ekström (2003), Simultaneous inversion for mantle shear velocity and topography of transition zone discontinuities, *Geophys. J. Int.*, *154*(2), 559–583, doi:10.1046/j.1365-246X.2003.01967.x.

Hier-Majumder, S., and B. Tauzin (2017), Pervasive upper mantle melting beneath the western US, *Earth Planet. Sci. Lett.*, *463*, 25–35, doi:10.1016/j.epsl.2016.12.041.

Hirschmann, M. M. (2006), Water, melting, and the deep Earth H_2O cycle, *Annu. Rev. Earth Planet. Sci.*, *34*(1), 629–653, doi:10.1146/annurev.earth.34.031405.125211.

Houser, C. (2016), Global seismic data reveal little water in the mantle transition zone, *Earth Planet. Sci. Lett.*, *448*, 94–101, doi:10.1016/j.epsl.2016.04.018.

Houser, C., G. Masters, M. Flanagan, and P. Shearer (2008), Determination and analysis of long-wavelength transition zone structure using *SS* precursors, *Geophys. J. Int.*, *174*(1), 178–194, doi:10.1111/j.1365-246X.2008.03719.x.

Huang, J., and S. Zhong (2005), Sublithospheric small-scale convection and its implications for the residual topography at old ocean basins and the plate model, *J. Geophys. Res.*, *110*, B05404, doi:10.1029/2004JB003153.
Huang, X., Y. Xu, and S.-i. Karato (2005), Water content in the transition zone from electrical conductivity of wadsleyite and ringwoodite, *Nature*, *434*(7034), 746–749.
Huckfeldt, M., A. M. Courtier, and G. M. Leahy (2013), Implications for the origin of Hawaiian volcanism from a converted wave analysis of the mantle transition zone, *Earth Planet. Sci. Lett.*, *373*, 194–204, doi:10.1016/j.epsl.2013.05.003.
Jasbinsek, J., and K. Dueker (2007), Ubiquitous low-velocity layer atop the 410-km discontinuity in the northern Rocky Mountains, *Geochem. Geophys. Geosyst.*, *8*, Q10004, doi:10.1029/2007GC001661.
Jasbinsek, J. J., K. G. Dueker, and S. M. Hansen (2010), Characterizing the 410 km discontinuity low-velocity layer beneath the LA RISTRA array in the North American Southwest, *Geochem. Geophys. Geosyst.*, *11*, Q03008, doi:10.1029/2009GC002836.
Kennett, B. L. N., and E. R. Engdahl (1991), Traveltimes for global earthquake location and phase identification, *Geophys. J. Int.*, *105*(2), 429–465, doi:10.1111/j.1365-246X.1991.tb06724.x.
Kohlstedt, D. L., H. Keppler, and D. C. Rubie (1996), Solubility of water in the α, β and γ phases of $(Mg,Fe)_2SiO_4$, *Contrib. Mineral. Petrol.*, *123*(4), 345–357, doi:10.1007/s004100050161.
Lawrence, J. F., and P. M. Shearer (2006), Constraining seismic velocity and density for the mantle transition zone with reflected and transmitted waveforms, *Geochem. Geophys. Geosyst.*, *7*, Q10012, doi:10.1029/2006GC001339.
Leahy, G. M., and D. Bercovici (2007), On the dynamics of a hydrous melt layer above the transition zone, *J. Geophys. Res.*, *112*, B07401, doi:10.1029/2006JB004631.
Leahy, G. M. (2009), Local variability in the 410-km mantle discontinuity under a hotspot, *Earth Planet. Sci. Lett.*, *288*(1–2), 158–163, doi:10.1016/j.epsl.2009.09.018.
Lebedev, S., and R. D. van der Hilst (2008), Global upper-mantle tomography with the automated multimode inversion of surface and *S*-wave forms, *Geophys. J. Int.*, *173*(2), 505–518, doi:10.1111/j.1365-246X.2008.03721.x.
Liu, Z., J. Park, and S.-i. Karato (2016), Seismological detection of low-velocity anomalies surrounding the mantle transition zone in Japan subduction zone, *Geophys. Res. Lett.*, *43*, 2480–2487, doi:10.1002/2015GL067097.
Montelli, R., G. Nolet, F. A. Dahlen, G. Masters, E. R. Engdahl, and S.-H. Hung (2004), Finite-frequency tomography reveals a variety of plumes in the mantle, *Science*, *303*(5656), 338–343, doi:10.1126/science.1092485.
Morais, I., L. Vinnik, G. Silveira, S. Kiselev, and L. Matias (2015), Mantle beneath the Gibraltar Arc from receiver functions, *Geophys. J. Int.*, *200*(2), 1155–1171, doi:10.1093/gji/ggu456.
Obayashi, M., H. Sugioka, J. Yoshimitsu, and Y. Fukao (2006), High temperature anomalies oceanward of subducting slabs at the 410-km discontinuity, *Earth Planet. Sci. Lett.*, *243*(1–2), 149–158, doi:10.1016/j.epsl.2005.12.032.
Parsons, B., and J. G. Sclater (1977), An analysis of the variation of ocean floor bathymetry and heat flow with age, *J. Geophys. Res.*, *82*(5), 803–827, doi:10.1029/JB082i005p00803.
Pearson, D. G., et al. (2014), Hydrous mantle transition zone indicated by ringwoodite included within diamond, *Nature*, *507*(7491), 221–224, doi:10.1038/nature13080.
Revenaugh, J., and S. A. Sipkin (1994), Seismic evidence for silicate melt atop the 410-km mantle discontinuity, *Nature*, *369*(6480), 474–476.
Ringwood, A. E. (1975), *Composition and Petrology of the Earth's Mantle*, p. 618, McGraw-Hill, New York.
Schaeffer, A. J., and M. G. Bostock (2010), A low-velocity zone atop the transition zone in northwestern Canada, *J. Geophys. Res.*, *115*, B06302, doi:10.1029/2009JB006856.
Schmandt, B., K. G. Dueker, S. M. Hansen, J. J. Jasbinsek, and Z. Zhang (2011), A sporadic low-velocity layer atop the western U.S. mantle transition zone and short-wavelength variations in transition zone discontinuities, *Geochem. Geophys. Geosyst.*, *12*, Q08014, doi:10.1029/2011GC003668.
Schmerr, N., and E. J. Garnero (2007), Upper mantle discontinuity topography from thermal and chemical heterogeneity, *Science*, *318*(5850), 623–626, doi:10.1126/science.1145962.
Schmerr, N. C., B. M. Kelly, and M. S. Thorne (2013), Broadband array observations of the 300 km seismic discontinuity, *Geophys. Res. Lett.*, *40*, 841–846, doi:10.1002/grl.50257.
Shearer, P. M. (1991), Imaging global body wave phases by stacking long-period seismograms, *J. Geophys. Res.*, *96*(B12), 20,353–20,364, doi:10.1029/91JB00421.
Shearer, P. M. (1996), Transition zone velocity gradients and the 520-km discontinuity, *J. Geophys. Res.*, *101*(B2), 3053–3066, doi:10.1029/95JB02812.
Song, T.-R. A., D. V. Helmberger, and S. P. Grand (2004), Low-velocity zone atop the 410-km seismic discontinuity in the northwestern United States, *Nature*, *427*(6974), 530–533, doi:10.1038/nature02231.
Takei, Y., F. Karasawa, and H. Yamauchi (2014), Temperature, grain size, and chemical controls on polycrystal anelasticity over a broad frequency range extending into the seismic range, *J. Geophys. Res. Solid Earth*, *119*, 5414–5443, doi:10.1002/2014JB011146.
Tauzin, B., E. Debayle, and G. Wittlinger (2010), Seismic evidence for a global low-velocity layer within the Earth's upper mantle, *Nat. Geosci.*, *3*(10), 718–721, doi:10.1038/ngeo969.
Tauzin, B., R. D. van der Hilst, G. Wittlinger, and Y. Ricard (2013), Multiple transition zone seismic discontinuities and low velocity layers below western United States, *J. Geophys. Res. Solid Earth*, *118*, 2307–2322, doi:10.1002/jgrb.50182.
Thio, V., L. Cobden, and J. Trampert (2016), Seismic signature of a hydrous mantle transition zone, *Phys. Earth Planet. Inter.*, *250*, 46–63, doi:10.1016/j.pepi.2015.11.005.
Thompson, D. A., J. O. S. Hammond, J. M. Kendall, G. W. Stuart, G. R. Helffrich, D. Keir, A. Ayele, and B. Goitom (2015), Hydrous upwelling across the mantle transition zone beneath the Afar Triple Junction, *Geochem. Geophys. Geosyst.*, *16*, 834–846, doi:10.1002/2014GC005648.
Toffelmier, D. A., and J. A. Tyburczy (2007), Electromagnetic detection of a 410-km-deep melt layer in the southwestern United States, *Nature*, *447*(7147), 991–994, doi:10.1038/nature05922.
van der Meijde, M., F. Marone, D. Giardini, and S. van der Lee (2003), Seismic evidence for water deep in Earth's upper mantle, *Science*, *300*(5625), 1556–1558, doi:10.1126/science.1083636.
Vinnik, L., and V. Farra (2002), Subcratonic low-velocity layer and flood basalts, *Geophys. Res. Lett.*, *29*(4), 1049, doi:10.1029/2001GL014064.
Vinnik, L., and V. Farra (2007), Low *S* velocity atop the 410-km discontinuity and mantle plumes, *Earth Planet. Sci. Lett.*, *262*(3–4), 398–412, doi:10.1016/j.epsl.2007.07.051.
Vinnik, L., M. Ravi Kumar, R. Kind, and V. Farra (2003), Super-deep low-velocity layer beneath the Arabian plate, *Geophys. Res. Lett.*, *30*(7), 1415, doi:10.1029/2002GL016590.
Vinnik, L., Y. Ren, E. Stutzmann, V. Farra, and S. Kiselev (2010), Observations of *S410p* and *S350p* phases at seismograph stations in California, *J. Geophys. Res.*, *115*, B05303, doi:10.1029/2009JB006582.

Wei, S. S., D. A. Wiens, Y. Zha, T. Plank, S. C. Webb, D. K. Blackman, R. A. Dunn, and J. A. Conder (2015), Seismic evidence of effects of water on melt transport in the Lau back-arc mantle, *Nature*, *518*(7539), 395–398, doi:10.1038/nature14113.

Wittlinger, G., and V. Farra (2007), Converted waves reveal a thick and layered tectosphere beneath the Kalahari super-craton, *Earth Planet. Sci. Lett.*, *254*(3–4), 404–415, doi:10.1016/j.epsl.2006.11.048.

Yamauchi, H., and Y. Takei (2016), Polycrystal anelasticity at near-solidus temperatures, *J. Geophys. Res. Solid Earth*, *121*, 7790–7820, doi:10.1002/2016JB013316.

Zhao, D., Y. Xu, D. A. Wiens, L. Dorman, J. Hildebrand, and S. Webb (1997), Depth extent of the Lau back-arc spreading center and its relation to subduction processes, *Science*, *278*(5336), 254–257, doi:10.1126/science.278.5336.254.

Zhu, H., E. Bozdağ, T. S. Duffy, and J. Tromp (2013), Seismic attenuation beneath Europe and the North Atlantic: Implications for water in the mantle, *Earth Planet. Sci. Lett.*, *381*, 1–11, doi:10.1016/j.epsl.2013.08.030.